JGR

RESEARCH ARTICLE

Key Points:
- Atmospheric ionization effects on aerosol scavenging are simulated
- Scavenging rate coefficients are parameterized
- Macroscopic effects for clouds are outlined

Correspondence to:
B. A. Tinsley,
tinsley@utdallas.edu

Parameterization of aerosol scavenging due to atmospheric ionization

Brian A. Tinsley[1] and Limin Zhou[2]

[1]Physics Department, University of Texas, Dallas, Texas, USA, [2]Key Laboratory of Geographic Information Science, East China Normal University, Shanghai, China

Abstract A new approach to parameterizing the modulation of aerosol scavenging by electric charges on particles and droplets gives improved accuracy and is applied over an extended range of droplet and particle radii relevant to cloud microphysical processes. The base level scavenging rates for small particles are dominated by diffusion and for large particles by intercept, weight, and flow effects. For charged particles encountering uncharged droplets, in all cases there is an increase in the scavenging rates, due to the image force. For droplets with charges of opposite sign to those of the particle charge, the rates are further increased, due to the Coulomb force, whereas for droplet with charges of the same sign, the rates are decreased. Increases above the base level (electroscavenging) predominate for the larger particles and occur in the interior of clouds even when no space charge (net charge) is present. Decreases below the base level (electroantiscavenging) occur for same-sign charges with smaller particles. The rates for uncharged droplets are parameterized, and the effect of charges on the droplets then parameterized as a departure from those rates. The results are convenient for incorporation in models of clouds which include detailed microphysics, to model the electrically induced reductions and increases in cloud condensation nucleus and ice forming nucleus concentrations and size distributions and contact ice nucleation rates that affect coagulation and precipitation and cloud albedo. Implications for effects on weather and climate, due both to externally and internally induced variability in atmospheric ionization, are outlined.

1. Introduction

1.1. Atmospheric Relevance

Changes in the concentrations and size distributions of aerosol particles acting as cloud condensation nuclei (CCN) and ice forming nuclei (IFN) are known to affect droplet size distributions and precipitation [e.g., *Tao et al.*, 2012], which in turn affect cloud cover and storm invigoration [e.g., *Rosenfeld et al.*, 2006, 2008]. Processes involved in production and loss of aerosol particles are active areas of research. Electric charge deposited on droplets and particles is known to affect aerosol loss processes, both from theoretical analyses and from a few laboratory experiments [*Pruppacher and Klett*, 1997, chap. 17]. Observed atmospheric responses to global atmospheric electrical variations [*Tinsley*, 2000; *Lam et al.*, 2013; *Burns et al.*, 2008; *Harrison and Ambaum*, 2013] may be due to this charge modulation of aerosol scavenging (abbreviated CMAS).

Atmospheric ions are produced by cosmic ray fluxes throughout the atmosphere, and attach to aerosol particles, with the ratios of positive/negative/neutral-charged particle concentrations dependent on the ratios for attachment and recombination. Typical values are given in Table 1 of *Zhou and Tinsley* [2007], based on the theory of *Keefe et al.* [1968] and *Hoppel and Frick* [1986]. At equilibrium the positive/neutral particle ratio is typically about one third, and the negative/neutral particle ratio is about one half. For zero space charge (zero net charge), the overall neutrality is ensured by a compensating asymmetry in the concentrations of positive and negative air ions. The downward flow of current in the global electric circuit, in the form of current density J_z (typically a few Pa/m^2), generates space charge in accordance with Poisson's equation as it flows through gradients of conductivity, generating gradients of electric field, at the boundaries of cloud, haze, and aerosol layers, so that positive space charge is generated at upper boundaries and negative space charge at lower boundaries. The space charge perturbs the positive/negative ratios, both for ions, aerosol particles, and for droplets.

For small particles (less than about 0.1 μm radius) the long-range Coulomb repulsion between like charged particles and droplets, or between small and larger aerosol particles, reduces scavenging and coagulation loss rates otherwise due to Brownian diffusion. Eventually, the concentration of the small particles in a cloud

or aerosol layer becomes larger than it would have been without the electric charge. Conversely, for large charged particles in clouds, the scavenging rate is increased by the short-range image force due to charge on the particle, with little effect of droplet charge. This causes a reduction of the concentration of these larger particles even in the interior of clouds, where there may be little space charge. The modeling of *Zhou and Tinsley* [2007, 2012] evaluated space charge accumulation for stable cloud layers, but did not include the effects of updrafts and downdrafts, and these would introduce air with space charge into cloud interiors.

The present results quantify and parameterize the effects of charge, in conjunction with diffusion, weight, intercept, and flow effects. The effects of phoretic scavenging have been evaluated previously [see *Tinsley and Leddon*, 2013, Figure 4] and are negligible for the smallest particles. For those of radii between 0.01 μm and 2 μm the phoretic scavenging during evaporation, with relative humidity decreasing from 100% to below 95%, is approximatively (arithmetically, not logarithmically) additive. For relative humidity up to at least 102% [*Tinsley and Leddon*, 2013, Figure 11] the phoretic reduction in scavenging during the condensation process is approximatively subtractive, leaving the charge effects as a greater fraction of the total.

The time scales for the response of droplet and particle charges to a change in ion concentration were found to range from about an hour to about a minute, being smaller at higher altitudes and larger for larger aerosol concentrations [*Zhou and Tinsley*, 2012]. The time scales for changes in aerosol concentrations by scavenging in clouds due to changes in charges on particles and droplets are a few hours [*Tinsley*, 2010]. The lifetimes of aerosol particles, and therefore of variations in size distribution, are 1–10 days [*Pruppacher and Jaenike*, 1995; *Pruppacher and Klett*, 1997, section 8.2.6]. The cumulative effects of CMAS create a new balance with aerosol production process, with changes in aerosol concentrations and size distribution throughout an air mass.

It is difficult to measure particle charges and the associated collision rate coefficients both within clouds and in the laboratory, especially as functions of particle radius, droplet charges, and droplet radii, but it is now possible to make comprehensive computer simulations of these. These can be used for evaluating the effects of atmospheric ionization on aerosol scavenging generally, especially for scavenging of cloud condensation nuclei (CCN) and ice forming nuclei (IFN) in cloud models with detailed microphysics.

1.2. Approach to Simulations

The book by *Young* [1993, pp. 88–93] gives theory and analytical results for modeling Brownian collection, thermophoresis, and diffusophoresis, as relevant to contact ice nucleation in clouds. The book by *Pruppacher and Klett* [1997] gives theory, analytical, numerical modeling, and laboratory results for Brownian, phoretic, and electrical charge modulation of scavenging. The analytical "flux" model is given for diffusion, phoretic, and inverse square electric effects, and the numerical "trajectory" model is for electrical effects combined with weight, inertia, and intercept effect (but not diffusion). The present work uses the trajectory model, and includes diffusion [*Tinsley*, 2010; *Tinsley and Leddon*, 2013] by means of a Monte Carlo technique, and the important noninverse square image force. It has been developed out of the nondiffusive treatment in *Tinsley et al.* [2006]. Further discussion of the use of the flux model, in parameterizing the base level (zero charge) rate coefficients, is given in section 2.2. To avoid lengthening this paper the theoretical basis given in our previous papers is not repeated here.

Trajectory simulations of scavenging with diffusion take large amounts of computer time (it has taken several years on workstations for the present extended set), and so parameterization of the scavenging rate coefficients is necessary for incorporating the rate coefficients into cloud models. A difficulty for previous simulations and parameterizations is that they have not been for the dominant droplet sizes in clouds [*Tripathi et al.*, 2006] or have been incomplete and complex to apply [*Tinsley and Leddon*, 2013]. The present work using a different approach is more complete, more accurate, and user friendly.

Flow around the larger particles [*Tinsley et al.*, 2006] affects the droplet trajectory, and this "*fap*" effect becomes significant for particle radii greater than about 10% of the radius of the droplet involved. Scavenging by 3 μm radius droplets of 1 μm radius particles is thus more affected by *fap* than scavenging of the same particles by 15 μm droplets. The correction for the *fap* effect, where relevant, was evaluated separately using the code of *Tinsley et al.* [2006] (which does not treat diffusion).

The rate coefficients are designated as $R_{Q,q,A,a}$, where Q is the droplet charge, q is the particle charge, A is the droplet radius, and a is the particle radius. Values of A used were 15 μm, 6 μm, and 3 μm, and values of a used were 0.004, 0.008, 0.01, 0.02, 0.04, 0.1, 0.2, 0.4, 1.0, 1.5, and 2.0 μm. The particle charges (q) were 0, 2, 5, 10, 20, and 50 e, and the droplet charges (Q) were 0, 25, 50, and 100 e for $A = 6$ μm; 0, 50, 100, and 200 e for $A = 15$ μm; and 0, 10, 25, and 50 e for $a = 3$ μm, where e is the elementary charge, and collisions of same-sign as well as opposite-sign charges were simulated. In this work the atmospheric pressure and temperature and relative humidity were 540 hPa, 256 K, and 100%, respectively, and the particle densities were 500 kg m^{-3}. The computational uncertainties of the present simulations are less than previously [*Tinsley and Leddon*, 2013], with the Monte Carlo statistical fluctuations at most ±2%, and less than 0.5% for larger particles for which the need to parameterize the smaller variations with Q required higher precision. This necessitated the use of a larger number of trials for trajectories (at each of a sequence of offsets from the vertical axis of symmetry), with runs for each rate coefficient taking up to several weeks, using two fast HP workstations. For the larger particles (0.3 μm $< a <$ 2 μm) with smaller charges ($q = 2\,e$ and $5\,e$) the differences in rate coefficients between charged and uncharged droplets and particles are smaller, and simulations with larger numbers of trials, to give about 200,000 collisions, were made to maintain adequate representation of the variations.

1.3. Relative Importance of Image and Coulomb Forces and Diffusion

The electrical force between charged aerosol particles and charged droplets is a combination of a Coulomb inverse square force, proportional to the product of Q and q, which is the dominant component for separations more than a few droplet radii, and the image charge forces that are important when the particle and droplet surfaces are within a few droplet radii of each other. The image forces are attractive, and that due to the charge q on the particle creates an opposite-sign image (actually an extended dipole) on the droplet with the force varying roughly as q^2, which depends strongly on the separation between the surface of the droplet and the center of the small particle. The droplet charge Q is located effectively at the distant droplet center, and its corresponding image force (creating an induced and essentially point dipole on the particle) is much weaker. For similar reasons, the particle image force is generally much stronger than the Coulomb force at small separations. For large particles, with radius a on the order of 1 μm, diffusion is small, and the image attractions are the dominant forces in ensuring a collision, when the particle would otherwise be carried past the droplet by the quasi-Stokes flow.

For small particles, diffusion ensures collisions in the absence of electrical forces, and it is the Coulomb force at large distances that dominates the modulation of the Brownian collision rates, with the Coulomb force attractive and increasing the collision (scavenging) rates for opposite-signed droplet and particle charges and repulsive and decreasing the rates for same-sign droplet and particle charges. The electrical forces are derived from the slowly converging series given by *Davis* [1964a, 1964b], which we have summed and coded into look-up tables for an extensive set of ratios of droplet to particle radii, where the ratio is less than 150, and which are used when particle and droplet centers are separated by less than 6 droplet radii. For the smallest particle/droplet ratios and largest separations the analytic expression of *Tinsley et al.* [2006] was used. To include cases where a large droplet charge creates an image on the largest particles, it is replaced by the analytic expression given by *Khain et al.* [2004]. For an example showing the relative accuracy of the *Khain et al.*'s [2004] treatment compared to that of *Davis* [1964a, 1964b], see *Tinsley and Zhou* [2014]. The *Davis* [1964a, 1964b] expressions can be used to include the forces due to electric fields, important in thunderstorms, but not important for weakly electrified clouds and haze layers, for which the present work is relevant.

1.4. Approach to Parameterization

The simulated $R_{Q,q,A,a}$ values are expressed as logarithmic ratios to the base level (uncharged) $R_{0,0,A,a}$ rate coefficients, because the use of logarithmic ratios, rather than absolute R values, provides better fitting in the parameterization, as there is much less variation of this ratio than in the R values. Thus,

$$F_{Q,q,A,a} = \log_{10}\left(R_{Q,q,A,a}/R_{0,0,A,a}\right) \tag{1}$$

Logarithms to the base 10 are used for convenience. The values of F are parameterized in the form of continuous polynomial functions fitted to the discrete values obtained in the simulations. A number of different ways of parameterizing the results of the simulations were tried, including that of *Tinsley and Leddon* [2013].
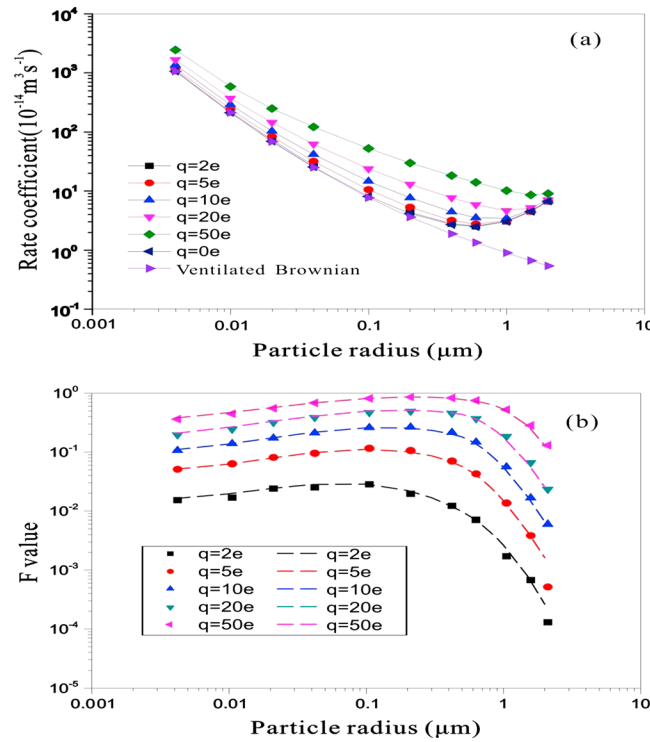
Figure 1. Results of simulations for droplet radii $A = 6$ with droplet charge $Q = 0$, particle radii a ranging from 0.004 μm to 2.0 μm, and particle charges q ranging from 2 e to 50 e, where e is the elementary charge. (a) The rate coefficients $R_{Q,q,A,a}$ in units of 10^{-14} m^3 s^{-1} are shown, together with those for the base level coefficients ($Q = q = 0$) in black and the ventilated Brownian (particles with zero radius and zero mass) coefficients in purple. (b) The values of the logarithmic ratio of the rate coefficients to the base level uncharged rate coefficient $R_{0,0,A,a}$, i.e., the ratio $F_{Q,q,A,a} = \log_{10}(R_{Q,q,A,a}/R_{0,0,A,a})$.

The most accurate way we have found is to parameterize the F values for zero Q with varying q and then treat the effects *of* Q as deviations from the rates for zero Q. This is particularly suitable for the relatively small effect of Q compared that of q for the larger particles.

The logarithmic ratios $F_{0,q,A,a}$ for nonzero q values taken with zero Q values are first obtained for discrete q values. These are parameterized as continuous functions $G_{0,q,A,a}$ fitted to the discrete values $F_{0,q,A,a}$. The effect of Q for a given q is next obtained by parameterizing the discrete differences ($F_{Q,q,A,a} - F_{0,q,A,a}$) by fitting continuous functions $H_{Q,q,A,a}$ to these differences. Then the continuous parameterized logarithmic ratios for both q and Q being nonzero are obtained by adding $H_{Q,q,A,a}$ to $G_{0,q,A,a}$.

A parameterization of the base level rate coefficients $R_{0,0,A,a}$ is made by fitting a continuous (nonlogarithmic) function $P_{0,0,A,a}$ to the discrete values of $R_{0,0,A,a}$. Then the general parameterized values $P_{Q,q,A,a}$ for the rate coefficients for nonzero particle and droplet charges can be evaluated rapidly, as needed in cloud models, i.e.,

$$P_{Q,q,A,a} = P_{0,0,A,a} \times 10^{**}(H_{Q,q,A,a} + G_{0,q,A,a}) \qquad (2)$$

When q or Q tends to zero, then G or H tends to zero, respectively, giving the accurate representation in the limits of small charges. The quality of the fits of the continuous parameterizations to the discrete simulations will be shown by overlaying the two sets of data in following figures. In addition, differences between the parameterizations and simulations will be quoted as percentages.

2. Results

2.1. *R* and *F* Values for Particle Encounters With Droplets of Zero *Q*

Figure 1a shows the variations of the results of the trajectory simulations for rate coefficients $R_{Q,q,A,a}$ with a, for $Q = 0$, $A = 6$ μm, q values from 0 to 50 e, and a ranging from 0.004 μm to 2.0 μm. The particle density is taken as 500 kg m^{-3} (specific gravity 0.5). The $P_{0,0,A,a}$ values for droplet charge $Q = 0$ with q from 2 e to 50 e are shown as color-coded curves. The $R_{0,0,A,a}$ curve (black) and the analytical Brownian curve (purple) coincide for $a < 0.1$ μm, but deviate for larger a owing to the combined effects of particle weight and intercept, and for $a > 1.0$ μm an increasing effect of *fap*. Figure 1b shows the variations of the ratio $F_{0,q,A,a}$ derived from the results shown in Figure 1a, using equation (1) and the values of $R_{0,0,A,a}$. It can be seen that there is much less variation in $F_{0,q,A,a}$ than in $R_{0,q,A,a}$ over most of the range.

2.2. Parameterization of Base Level Rate Coefficients

The simulated rate coefficients for zero charges, $R_{0,0,A,a}$, provide the base level for the parameterization of those with nonzero charge. For continuous functions fitted to these discrete rate coefficients, for use with

equation (2), it is convenient to define the function $P_{0,0,A,a}$ as the sum of two terms: the first for diffusion, R_F, including any phoretic (droplet evaporation or condensation) effects if the relative humidity is other than 100%, and a second term, P_C, for combined effects of particle weight, intercept, and fap. Then P_C is obtained by fitting it to the discrete values of $R_{0,0,A,a}$ minus the diffusion term. Thus,

$$P_{C,A,a} = R_{0,0,A,a} - R_{F,A,a} \tag{3}$$

The term R_F is known as the flux expression:

$$R_F = 4\pi B_p C / \big(\exp\big(B_p C / (D_p f_p A)\big) - 1\big) \tag{4}$$

This expression was used by *Wang et al.* [1978] and *Pruppacher and Klett* [1997, section 18.6.6] for obtaining scavenging rate coefficients with diffusion, phoretic, and electric forces, but it only applies for inverse square electric forces, which are a poor approximation for the present work. However, the expression is useful for the term R_F with zero charge in the base level curve, accounting for diffusion and phoretic effects, as in *Pruppacher and Klett* [1997, section 17.4.2.5]. $R_{0,0,A,a}$ includes the effect of weight, intercept, and fap, that are important for larger particles and must be determined from the simulations. In equation (4) A is the droplet radius, B_p is the mobility of the particle and is related to D_p, the diffusion coefficient for particles of radius a, by the Einstein relation $B_p = D_p / kT$. The absolute temperature is T and k is the Boltzmann's constant. Expressions giving D_p in terms of the selected atmospheric pressure, density, and temperature for a given particle radius a are given in the Appendix to *Tinsley et al.* [2006]. The factor f_p is the particle ventilation factor, and its variation with a is determined from comparing simulations for particles with diffusion coefficient, determined by particle radius a, colliding with the falling (ventilated) droplet, (but excluding the effects of weight and intercept and other effects for larger particles) with the expression for collisions with a stationary droplet. A first approximation to f_p was given by *Pruppacher and Klett* [1997, section 17.4.2.1], and the expression from the simulation of *Tinsley* [2010] has been improved in accuracy in the present work, and is

$$f_p = 1 + 0.530N \exp(-1.1/N) \tag{5}$$

where N is the cube root of the Péclet number, i.e.,

$$N = \big(2U_\infty A / D_p\big)^{1/3} \tag{6}$$

where U_∞ is the fall speed of the droplet relative to undisturbed air, given as a function of air density by *Beard and Pruppacher* [1969] [see *Pruppacher and Klett*, 1997, section 10.3.7]. The value of C in equation (4) is used here as only due only to any phoretic forces, and $C = C_{Th} + C_{Df}$, where C_{Th} and C_{Df} represent the ventilated thermophoretic and diffusophoretic force constants, with expressions given by *Young* [1993, pp. 88–93] and *Pruppacher and Klett* [1997, section 17.4.2.5]. The terms with numerical values for these expressions are given in the Appendix to *Tinsley et al.* [2006]. For the case of $C = 0$, or only ventilated Brownian collection, equation (4) becomes

$$R_F = 4\pi D_p f_p A \tag{7}$$

(The expression for a stationary droplet is $R_F = 4\pi D_p A$.) As noted, the term $P_{C,A,a}$ in the parameterization of $R_{0,0,A,a}$ that accounts for particle weight, intercept, and fap is evaluated by taking the difference between the simulations of the discrete $R_{0,0,A,a}$ values, as in Figure 1a, and the analytical flux expressions (4) or (7), i.e., the differences $(R_{0,0,A,a} - R_{F,A,a})$ as in equation (3). Then a least squares fitting for $P_{C,A,a}$ is made to the sets of differences, separately for each droplet size. The results of such fitting, in units of $10^{-14}\,\mathrm{m^3\,s^{-1}}$, with a in μm are as follows:

$$\text{For } A = 3 \ \mu\text{m}; \qquad P_{C,3,a} = 0.605a - 0.137a^2 + 0.115a^3 \tag{8}$$

$$\text{For } A = 6 \ \mu\text{m}; \qquad P_{C,6,a} = 2.038a - 0.306a^2 + 0.412a^3 \tag{9}$$

$$\text{For } A = 15 \ \mu\text{m}; \qquad P_{C,15,a} = 10.970a - 0.291a^2 + 2.256a^3 \tag{10}$$

The above expressions can be further parameterized for the three values of A (exact fits at 3, 6, and 15 μm):

$$ba + ca^2 + da^3 = P_{C,A,a} \tag{11}$$

where

$$b = -0.05583 + 0.09158A + 0.04290A^2 \tag{12}$$

$$c = 0.11900 - 0.09983A + 0.00483A^2 \tag{13}$$

$$d = -0.02137 + 0.01958A + 0.00882A^2 \tag{14}$$

Table 1. Results for $A = 6\,\mu m$ for 11 Values of a of Fitted Parameters for the Variation of log $(F_{0,q,A,a})$ With log q as in Equation (16)

a (μm)	K	L	M	N
2.0	−4.134	1.747	0.371	−0.162
1.5	−3.609	1.571	0.459	−0.189
1.0	−3.058	1.386	0.825	−0.399
0.6	−2.702	1.864	0.291	−0.292
0.4	−2.540	2.182	−0.168	−0.156
0.2	−2.228	2.061	−0.344	−0.072
0.1	−2.064	1.812	−0.277	−0.064
0.04	−2.002	1.453	−0.002	−0.129
0.02	−2.025	1.348	0.042	−0.132
0.01	−2.109	1.361	−0.006	−0.110
0.004	−2.198	1.330	−0.010	−0.098

so that finally the continuous parameterized rate coefficient for zero charges is

$$P_{0,0,A,a} = P_{C,A,a} + R_{F,A,a} \tag{15}$$

2.3. Parameterizing Rate Coefficient Ratios for Encounters With Droplets of Zero Q

For Q of zero with nonzero q, the discrete logarithmic ratios $F_{0,q,A,a}$ are obtained from the simulations as described in the Introduction. These values for $A = 6\,\mu m$ are plotted in Figure 1b. Then continuous functions are fitted to the discrete $F_{0,q,A,a}$ values at each value of a. As can be seen in Figure 1 there are 11 discrete values of a (from 0.004 μm to 2.0 μm), so for each droplet radius A there will be 11 functions of q. A suitable functional form is to fit cubic functions of $\log_{10} q$ to the discrete $\log_{10} F_{0,q,A,a}$ values. Thus, we fit

$$K + L(\log q) + M(\log q)^2 + N(\log q)^3 = \log(F_{0,q,A,a}) \tag{16}$$

These $(F_{0,q,A,a})$ values are due to the image charge force alone. The flux expression treats only the Coulomb force which would give zero in these cases.

2.3.1. Results for Zero Q for $A = 6\,\mu m$

Table 1 lists for individual a values the results of the fitting for K, L, M, and N for $A = 6\,\mu m$.

Given K, L, M, and N for each discrete particle radius as in Table 1, the continuous expressions that define $G_{0,q,A,a}$ are

$$G_{0,q,A,a} = 10^{**}\left(K + L(\log q) + M(\log q)^2 + N(\log q)^3\right) \tag{17}$$

The quality of the fitting of $G_{0,q,A,a}$ in equation (17) to the corresponding $F_{0,q,A,a}$ can be seen in Figure 1b by comparing the fitted values from equation (17) (heavier dashed lines) to the individual point values of $F_{0,q,A,a}$. The statistical fluctuations are larger for the smaller values of q (e.g., $q = 2\,e$) because the differences between the R values, each with their inherent statistical fluctuations, are smaller. The fluctuations are also larger with smaller differences between R values for the larger particle sizes (e.g., $a > 0.04\,\mu m$). The average standard deviation for all q for a between 0.004 μm and 0.04 μm averages 0.85%. For the larger particles (0.04 $\mu m < a < 2\,\mu m$) the standard deviations average 2.16%.

It is possible to parameterize the coefficients K, L, M, and N as continuous functions of a. However, in order to preserve the accuracy of the simulations, it was found necessary to divide the range of a into two sections, because of a sharp change of slope of some of the curves near $a = 0.4\,\mu m$. The sections thus are 2 μm to 0.4 μm and 0.4 μm to 0.004 μm.

For $A = 6\,\mu m$ and for a between 2 μm and 0.4 μm the fitted expressions as functions of a for K, L, M, and N are

$$K = -3.070 - 2.337\log a - 3.386(\log a)^2 - 2.127(\log a)^3 \tag{18}$$

$$L = 1.468 - 0.807\log a + 4.560(\log a)^2 + 5.001(\log a)^3 \tag{19}$$

$$M = 0.685 + 0.350\log a - 4.942(\log a)^2 - 0.721(\log a)^3 \tag{20}$$

$$N = -0.341 + 0.334\log a + 1.509(\log a)^2 - 1.402(\log a)^3 \tag{21}$$

For $A = 6\,\mu m$ and for a between 0.4 μm and 0.004 μm the fitted expressions for K, L, M, and N as functions of a are

$$K = -3.212 - 2.124\log a - 1.162(\log a)^2 - 0.189(\log a)^3 \tag{22}$$

$$L = 2.381 + 0.258\log a - 0.512(\log a)^2 - 0.184(\log a)^3 \tag{23}$$

$$M = 0.217 + 1.574\log a + 1.464(\log a)^2 + 0.355(\log a)^3 \tag{24}$$

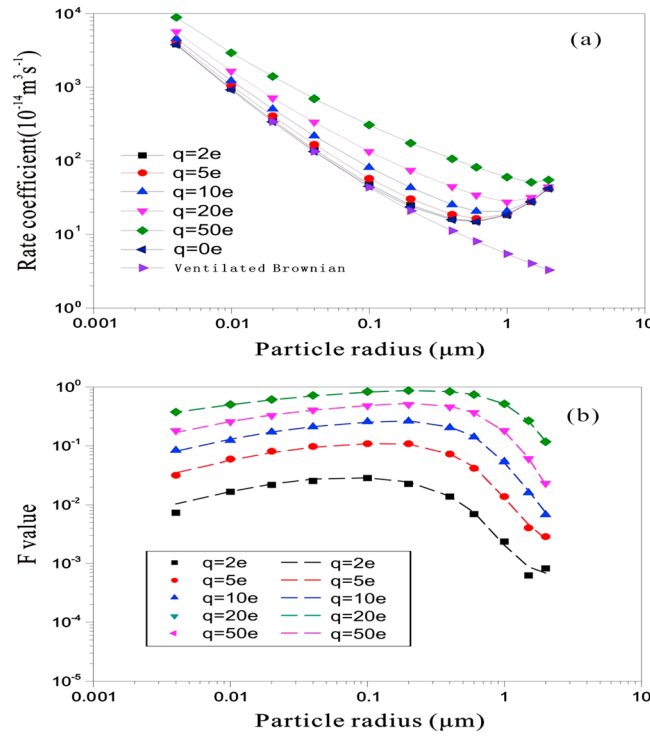$$N = -0.338 - 0.671\log a - 0.529(\log a)^2 - 0.122(\log a)^3 \tag{25}$$

Figure 2. Results of simulations for $A = 15\,\mu m$ in the same format as in Figure 1.

2.3.2. Results for Zero Q for A = 15 μm

In Figure 2 the results for $A = 15\,\mu m$ for the logarithmic ratios $F_{0,q,A,a}$ (Q of zero with nonzero q) are shown, in the same format as those in Figure 1 for $6\,\mu m$.

Table 2 lists for individual a values the results of the fitting for K, L, M, and N for $A = 15\,\mu m$.

The quality of the fitting of $G_{0,q,A,a}$ in equation (17) to the corresponding $F_{0,q,A,a}$ can be seen in Figure 2b by comparing the fitted values from equation (17) (heavier dashed lines) to the individual point values of $F_{0,q,A,a}$. As before, the statistical fluctuations are larger for the smaller values of q (e.g., $q = 2e$) and are larger for the larger particle sizes (e.g., $a > 0.04\,\mu m$). The average standard deviation for all q for a between $0.004\,\mu m$ and $0.04\,\mu m$ averages 2.4%. For the larger particles ($0.04\,\mu m < a < 2\,\mu m$) the standard deviations average 3.1%.

For $A = 15\,\mu m$ and for a between $2.0\,\mu m$ and $0.4\,\mu m$ the fitted expressions as for K, L, M, and N as functions of a are

$$K = -3.219 - 1.961 \log a + 1.114 (\log a)^2 + 2.752 (\log a)^3 \tag{26}$$

$$L = 1.576 - 2.529 \log a + 3.403 (\log a)^2 - 19.168 (\log a)^3 \tag{27}$$

$$M = 0.748 + 2.389 \log a - 10.517 (\log a)^2 - 30.319 (\log a)^3 \tag{28}$$

$$N = -0.336 - 0.259 \log a + 1.597 (\log a)^2 - 3.483 (\log a)^3 \tag{29}$$

For $A = 15\,\mu m$ and for a between $0.4\,\mu m$ and $0.004\,\mu m$ the fitted expressions for K, L, M, and N as functions of a are

$$K = -3.006 - 1.811 \log a - 0.964 (\log a)^2 - 0.130 (\log a)^3 \tag{30}$$

$$L = 2.004 - 0.300 \log a - 0.489 (\log a)^2 - 0.160 (\log a)^3 \tag{31}$$

$$M = 0.476 + 1.711 \log a + 1.377 (\log a)^2 + 0.319 (\log a)^3 \tag{32}$$

$$N = 0.390 - 0.671 \log a - 0.485 (\log a)^2 - 0.111 (\log a)^3 \tag{33}$$

Table 2. Results for $A = 15\,\mu m$ for 11 Values of a of Fitted Parameters for the Variation of log ($F_{0,q,A,a}$) With log q as in Equation (16)

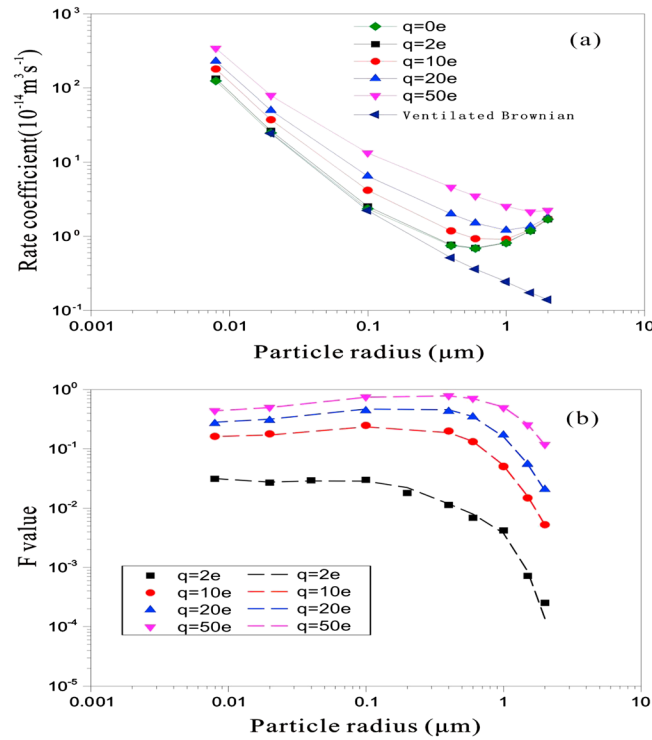| a (μm)	K	L	M	N
2.0	−3.612	1.649	−0.344	0.179
1.5	−3.570	1.330	0.762	−0.300
1.0	−3.158	1.587	0.656	−0.350
0.6	−2.793	2.089	0.084	−0.230
0.4	−2.425	1.915	0.027	−0.202
0.2	−2.181	1.926	−0.234	−0.099
0.1	−2.011	1.665	−0.151	−0.094
0.04	−2.009	1.483	−0.033	−0.115
0.02	−2.073	1.443	−0.036	−0.101
0.01	−2.194	1.422	−0.022	−0.093
0.004	−2.408	1.454	−0.083	−0.050

Figure 3. Results of simulations for $A = 3\,\mu m$ in the same format as in Figures 1 and 2.

2.3.3. Results for Zero Q for $A = 3\,\mu m$

In Figure 3 the results for $A = 3\,\mu m$ for the logarithmic ratios $F_{0,q,A,a}$ (Q of zero with nonzero q) are shown, in the same format as those in Figure 1 for $6\,\mu m$. It was not found necessary to make simulations for a values of 0.2, 0.04, 0.01, and 0.004 μm in view of the smoothness of the variations. A simulation was made for the a value of 0.008 μm rather than 0.004 μm, in view of the increasingly long computer simulation times with the smallest Péclet numbers (because of the smaller product of droplet radius and fall speed divided by the larger diffusion coefficients for the smallest particles).

Table 3 lists for individual a values the results of the fitting for K, L, M, and N for $A = 3\,\mu m$.

For $A = 3\,\mu m$ the overall fits of $G_{0,q,A,a}$ in equation (17) to the corresponding $F_{0,q,A,a}$ have standard deviations averaging 0.43% for a between 0.008 μm and 0.4 μm. For the larger particles (0.4 $\mu m < a < 2\,\mu m$) the standard deviations average 0.9%.

For $A = 3\,\mu m$ and for a between 2.0 μm and 0.4 μm the fitted expressions as for K, L, M, and N as functions of a are

$$K = -2.784 - 2.328 \log a - 9.484 (\log a)^2 - 14.775 (\log a)^3 \tag{34}$$

$$L = 0.986 - 0.138 \log a + 15.482 (\log a)^2 - 32.391 (\log a)^3 \tag{35}$$

$$M = 0.859 - 0.621 \log a - 11.786 (\log a)^2 - 22.677 (\log a)^3 \tag{36}$$

$$N = -0.340 + 0.664 \log a + 2.995 (\log a)^2 + 4.655 (\log a)^3 \tag{37}$$

For $A = 3\,\mu m$ and for a between 0.4 μm and 0.008 μm the fitted expressions for K, L, M, and N as functions of a are

$$K = -3.303 - 3.001 \log a - 2.081 (\log a)^2 - 0.471 (\log a)^3 \tag{38}$$

$$L = 1.963 + 1.710 \log a + 1.092 (\log a)^2 + 0.241 (\log a)^3 \tag{39}$$

$$M = 0.830 + 0.511 \log a + 0.188 (\log a)^2 + 0.397 (\log a)^3 \tag{40}$$

$$N = -0.549 - 0.410 \log a - 0.199 (\log a)^2 - 0.043 (\log a)^3 \tag{41}$$

Table 3. Results for $A = 3\,\mu m$ for Eight Values of a of Fitted Parameters for the Variation of $\log(F_{0,q,A,a})$ With $\log q$ as in Equation (16)

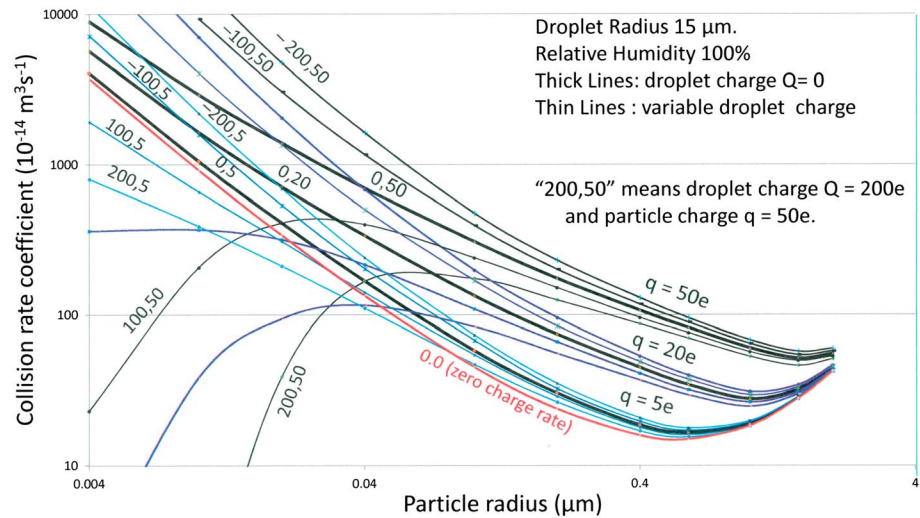| a (μm)	K	L	M	N
2.0	−4.701	3.205	−1.049	0.275
1.5	−3.695	1.691	0.342	−0.152
1.0	−2.648	0.909	0.772	−0.290
0.6	−2.651	1.470	0.715	−0.420
0.4	−2.406	1.440	0.654	−0.415
0.1	−1.905	1.104	0.467	−0.295
0.02	−1.889	1.029	0.309	−0.215
0.008	−1.802	0.959	0.218	−0.166

Figure 4. Results of simulations for $A = 15\,\mu m$ that include nonzero droplet charges. The format is similar to those of Figure 2a but for just three particle charges q of $5\,e$, $20\,e$, and $50\,e$. The heavy black lines are for droplet charge $Q = 0\,e$. For nonzero droplet charges, the rate coefficients for both positive and negative Q values of $100\,e$ and $200\,e$ are shown as light lines. The line for q and Q both zero (the base level curve) is the heavy red line.

2.4. R and F Values for Particle Encounters With Droplets of Nonzero Q

Figure 4 shows results for $A = 15\,\mu m$ in similar format to Figure 2a, for just three particle charges q of $5\,e$, $20\,e$, and $50\,e$, for droplet charge Q of zero in heavy black lines, together with results for nonzero Q (positive and negative droplet charges of $200\,e$ and $100\,e$) as light lines. The curve for q and Q both zero is the heavy red curve. For zero droplet charge the collision rate coefficient increases in all cases, due to the short-range attractive force between the charge on the particle and its image on the droplet, as noted earlier. The effect of droplet charge Q is to provide an additional Coulomb inverse square force, attractive or repulsive depending on whether Q and q have unlike or like signs. With the magnitude of the charges used here, the effect of Q is small for particles larger than about $0.3\,\mu m$ radius but becomes large and dominant with smaller and smaller particle radii. The same 11 values of a are used here as before, and for each of the 11 values of a and 5 values of q used in the simulations it is possible, as noted earlier, to treat the effect of droplet charges Q as creating differences $(F_{Q,q,A,a} - F_{0,q,A,a})$ which are functions of Q, with $F_{Q,q,A,a}$ being the rate coefficient for both Q and q nonzero. We regard here encounters between particles and droplets with like-sign charges as being for positive q and positive Q and encounters for unlike charges as positive q and negative Q.

In Figure 5 the results for $F_{Q,q,A,a}$ are given in color code for just three values of a, $0.01\,\mu m$, $0.04\,\mu m$, and $1.5\,\mu m$, for droplets of $A = 6\,\mu m$. The horizontal axis on each panel is the range of Q from $-100\,e$ to $+100\,e$, and the vertical axis is q from $1\,e$ to $50\,e$. On the central vertical lines in each of the three plots are values for $Q = 0$, corresponding to the analysis of section 2.3.1. The panels show Q-q planes at the three selected a values, with the colors showing how the increases and decreases in the rate coefficients occur with q, Q, and a. Note that the colors representing F values change from panel to panel. For $a = 1.5\,\mu m$ with the larger values of q the values of F are mostly positive, reflecting the effect of the particle-induced image force, with only a small tilt of the contours due to Q. The tilt increases with decreasing particle size, and by $a = 0.01\,\mu m$ most of the F values for positive Q are negative (electroantiscavenging) due to long-range Coulomb repulsion reducing diffusive scavenging, whereas for negative Q the F values are positive (electroscavenging) as the long-range Coulomb attraction increases scavenging. The F values for $q = 1\,e$ are obtained by interpolation between those for $q = 2\,e$ and $q = 0\,e$. The F values for Q nonzero (e.g., $Q = 100\,e$) with $q = 0\,e$ are not zero for the large particles of $a = 1.5\,\mu m$ and $a = 2\,\mu m$, because although the force due to the particle image charge and the Coulomb force are both zero, the force due to the dipole induced by Q on the larger particles is not. This effect can be seen in the light blue area (F value 0 to 0.05) for smaller q and larger Q in the lower right of the plot for $a = 1.5\,\mu m$ in Figure 5. The effect is present for larger q but becomes masked by the increasing effects of the repulsive Coulomb force.
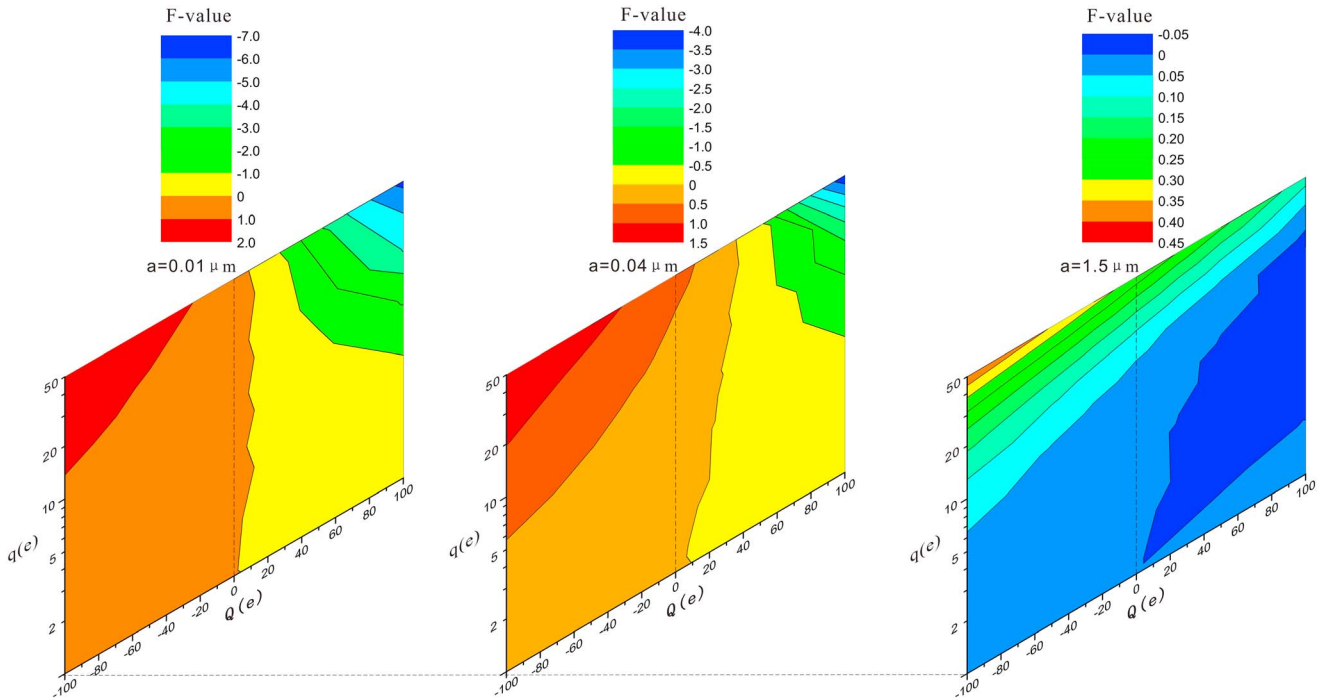
Figure 5. The variation with Q and q of $F_{Q,q,A,a}$ (the logarithmic ratio of the rate coefficients to the base rate coefficients) for just three values of a, 0.01 μm, 0.04 μm, and 1.5 μm, for droplets of $A = 6$ μm The panels show Q-q planes at the three selected a values, with color codes to show the increases and decreases in the rate coefficients with q, Q, and a. The horizontal axis on each panel is the range of Q from $-100\,e$ to $+100\,e$, and the vertical axis is q from $1\,e$ to $50\,e$. On the central vertical lines in each of the three plots are values for $Q = 0$, corresponding to the data of Figure 1b. Note that the colors representing F values change from panel to panel.

Figure 6 shows results for $A = 3$ μm in similar format to Figure 3a, for just two particle charges q of $10\,e$ and $50\,e$, for droplet charge Q of zero in heavy black lines, together with results for nonzero Q (positive and negative droplet charges of $25\,e$ and $10\,e$) as light lines. The curve for q and Q both zero is the heavy red curve.

2.5. Parameterizing the Perturbations Due to Q

Fitted expressions, $H_{Q,q,A,a}$, for the differential effect on F due to Q at each of the values (e.g., $0\,e$ to $50\,e$) of q for each of the values of a in the simulations were made in the form:

$$H_{Q,q,A,a} = S_1 \times 10^{-5} Q + S_2 \times 10^{-7} Q^2 + S_3 \times 10^{-9} Q^3 = F_{Q,q,A,a} - F_{0,q,A,a} \qquad (42)$$

where S_1, S_2, and S_3 are the functions of q, a, and A. This fitting ensures zero values of $H_{Q,q,A,a}$ when $Q = 0$, consistent with the zero value of the RHS in this case. Also, the fitting was done in such a way as to force a zero value of S_1 with $q = 0$, consistent with zero Coulomb force. S_2 is not zero with $q = 0$, as the image force produced by Q gives an attractive force, and as noted earlier it is an approximate function of Q^2 and is significant for the largest particles. However, S_3 was found to be zero for small q. After a complete set of simulations was made to generate Figure 5, and a preliminary fitting made for $H_{Q,q,A,a}$ with quadratic and cubic equations, it was found that the statistical fluctuations due to the Monte Carlo simulation of diffusion gave relatively large standard deviations with respect to differences between points in the fitted curves. Therefore, new simulations with much higher numbers of trials were made. The preliminary fitting showed that the terms in Q^3 were negligible for $a > 0.04$ μm for $A = 15$ μm, for $a > 0.2$ μm for A of 6 μm, and for $a > 0.4$ μm for A of 3 μm, and thus, for these it was only necessary to make and use results of repeat simulations for $Q = 0\,e$, $200\,e$, and $-200\,e$ for $A = 15$ μm; $Q = 0\,e$, $100\,e$, and $-100\,e$ for $A = 6$ μm; and $Q = 0\,e$, $50\,e$, and $-50\,e$ for $A = 3$ μm. However, for the smaller values of a, the seven values of Q were used to evaluate the Q^3 terms. (The repeat simulations for $Q = 0$ were also used to evaluate $G_{0,q,A,a}$.) The discrete values for $R_{Q,q,A,a}$ from the repeat simulations for $A = 15$ μm, 6 μm, and 3 μm are given as Tables A1, A2, and A3 as Appendix A. A few values for the smallest particles with the largest same-sign charges had collision rates too small to be of easily simulated, and values are approximate or omitted.
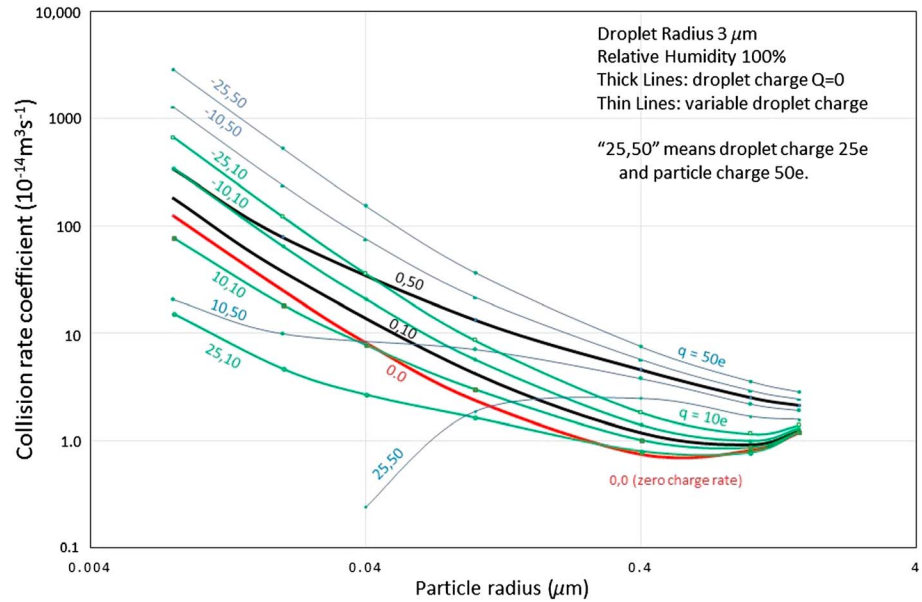
Figure 6. Results of simulations for $A = 3$ μm that include nonzero droplet charges. The format is similar to that of Figure 3a but for just two particle charges q of 10 e and 50 e. The heavy black lines are for droplet charges $Q = 0$ e. For nonzero droplet charges the rate coefficients for both positive and negative Q values of 10 e and 25 e are shown as green lines. The line for q and Q both zero (the base level curve) is the heavy red line.

The fitting is done with the discrete values of $F_{0,0,A,a}$ rather than the parameterized $G_{0,q,A,a}$ values, so that the parameterizations $H_{Q,q,A,a}$ of droplet charge effects are independent of small parameterizing errors in $G_{0,q,A,a}$ and are accurate for the differential effects as Q and q tend to zero. S_1 is always negative, as the rate coefficients always decrease with increasing Q (increasing like-sign charge), and a better fitting was obtained using $\log(-S_1)$ than with S_1. The $\log(-S_1)$ and S_2 values in turn can be parameterized as polynomial functions of $(\log q)$ fitted to 11 or 8 values of a as designated earlier. However, the values of S_3 (for Q^3) varied so rapidly that a parameterization in terms of exponentials was more suitable. The fitting is thus

$$U_1 + V_1(\log q) + W_1(\log q)^2 = \log(-S_1) \tag{43}$$

$$U_2 + V_2(\log q) + W_2(\log q)^2 + X_2(\log q)^3 = S_2 \tag{44}$$

$$U_3 \times q^{**}(V_3) \times 10^{**}(q/W_3) = S_3 \tag{45}$$

The choice of expression (45) was made to give zero values for S_3 for q of zero and after trials of other expressions were made that gave poorer fitting. Also, the values for S_3 were too small to be evaluated for the larger values of a as noted earlier and are represented by $U_3 = 0$. Then the continuous expressions $H_{Q,q,A,a}$ are given by

$$H_{Q,q,A,a} = -10^{-5}Q\left(10^{**}\left(U_1 + V_1(\log q) + W_1(\log q)^2\right)\right) + 10^{-7}Q^2\left(U_2 + V_2(\log q) + W_2(\log q)^2\right) + \\ 10^{-9}Q^3\left(U_3 \times q^{**}(V_3) \times 10^{**}(q/W_3)\right) \tag{46}$$

2.5.1. Results for U, V, and W for $A = 6$ μm

Table 4 gives the discrete results for U, V, W, and X for $A = 6$ μm.

To complete the parameterization for a given A, each of U, V, and W are expressed as continuous functions of a. To ensure more accurate representation of the small or zero values of S_2 and S_3 for the range of a of 2 to 0.4 μm compared to the larger values in the range of 0.4 to 0.004 μm, the parameterizations as functions of a for S_1, S_2, and S_3 have been made separately for the two ranges. For $A = 6$ μm and for a between 2.0 μm and 0.4 μm the fitted expressions as functions of a for U, V, W, and X are

From S_1:

$$U_1 = 1.019 - 1.636 \log a - 0.860(\log a)^2 + 0.983(\log a)^3 \tag{47}$$

$$V_1 = 1.149 - 0.039 \log a - 0.471(\log a)^2 + 0.092(\log a)^3 \tag{48}$$

$$W_1 = -0.240 + 0.469 \log a + 0.306(\log a)^2 - 1.146(\log a)^3 \tag{49}$$

Table 4. Results for $A = 6\ \mu m$ for the Fitted Parameters for the Continuous Variations of $\log(-S_1)$ as Functions of q in Terms of U_1, V_1, and W_1; of S_2 in Terms of U_2, V_2, W_2, and X_2; and of S_3 in Terms of U_3, V_3, and W_3 as in Equations (43)–(45)[a]

$a(\mu m)$	U_1	V_1	W_1	U_2	V_2	W_2	X_2	U_3	V_3	W_3
2.0	0.481	1.097	−0.105	10.7	−2.73	7.62	−6.07	0	-	-
1.5	0.695	1.129	−0.146	9.8	−3.41	12.0	−10.6	0	-	-
1.0	1.035	1.149	-0.248	5.7	3.26	−9.99	−0.62	0	-	-
0.6	1.320	1.134	−0.311	3.0	9.40	−35.6	10.4	0	-	-
0.4	1.475	1.084	−0.307	0.3	9.62	−41.8	11.9	0	-	-
0.2	1.645	1.128	−0.338	−1.8	16.3	−71.8	15.3	−0.0042	2.731	−59.15
0.1	1.806	1.113	−0.311	−3.2	19.2	−71.1	−25.5	−0.0211	2.731	−59.15
0.04	2.009	1.089	−0.253	−5.5	2.35	3.37	−240	−0.0622	2.731	−59.15
0.02	2.145	1.054	−0.190	−9.0	−36.7	132	−564	−0.1699	2.731	−59.15
0.01	2.260	1.021	−0.155	−14.7	−247	919	−1470	−0.3764	2.731	−59.15
0.004	2.338	1.005	−0.124	−21.4	−859	3124	−3330	−0.8575	2.731	−59.15

[a]Indeterminate results are indicated by the hyphen symbol. The values of S_2 and S_3 are second- and third-order terms in the fitting and for the smallest q values and the largest a values and have relatively greater statistical fluctuations. For S_2 the values for the smallest q have been smoothed with respect to (log a), as also were the values of S_3 for $q = 50\ e$. The remaining fitting for S_3 is determined by smoothing, for trends toward zero for the smallest q values and the largest a values, from the largest q values and the smallest a values, taking V_3 and W_3 as constants. The overall fits of $H_{Q,q,A,a}$ in the of range $2\ \mu m$ to $0.004\ \mu m$ to the corresponding $F_{Q,q,A,a} - F_{0,q,A,a}$ using equation (46) have standard deviations averaging 7.6%. For $a > 0.4\ \mu m$ the fits for S_1 and S_2 are made for Q values of $-100\ e$, $0\ e$, and $100\ e$, for each q are exact; however, the U, V, and W fitted as functions of q are not exact.

From S_2:

$$U_2 = 6.323 + 17.207 \log a - 1.186(\log a)^2 - 17.703(\log a)^3 \tag{50}$$

$$V_2 = 2.536 - 37.626 \log a + 14.744(\log a)^2 + 164.15(\log a)^3 \tag{51}$$

$$W_2 = -7.842 + 137.22 \log a - 100.66(\log a)^2 - 586.28(\log a)^3 \tag{52}$$

$$X_2 = -1.977 - 62.21 \log a + 58.83(\log a)^2 + 324.03(\log a)^3 \tag{53}$$

From S_3: the values for U_3 are zero in this range, and the values for V_3 and W_3 are indeterminate and irrelevant.

For $A = 6\ \mu m$ and for a between $0.4\ \mu m$ and $0.004\ \mu m$ there is a rapid increase in S_2 and S_3 with decreasing a. This was captured more accurately for S_2 for V_2 and W_2 by fitting to the products $(V_2 \times a)$ and $(W_2 \times a)$ and $(X_2 \times a)$ instead of just V_2, W_2, and X_2. For S_3 it was captured by using the expression (45) for U_3, V_3, and W_3. The fitting was to the product $(U_3 \times a)$ and to V_3 and W_3. The fitted expressions as functions of a for this range, for U, V, W, and X, are

From S_1:

$$U_1 = 1.278 - 0.460 \log a + 0.122(\log a)^2 + 0.054(\log a)^3 \tag{54}$$

$$V_1 = 0.971 - 0.412 \log a - 0.332(\log a)^2 - 0.069(\log a)^3 \tag{55}$$

$$W_1 = -0.189 + 0.457 \log a + 0.424(\log a)^2 + 0.093(\log a)^3 \tag{56}$$

From S_2:

$$U_2 = 1.747 + 4.582 \log a + 1.253(\log a)^2 + 1.425(\log a)^3 \tag{57}$$

$$V_2 = \left(4.276 - 0.334 \log a - 3.486(\log a)^2 - 0.836(\log a)^3\right)/a \tag{58}$$

$$W_2 = \left(-20.774 - 5.388 \log a + 10.256(\log a)^2 + 2.791(\log a)^3\right)/a \tag{59}$$

$$X_2 = \left(5.589 - 5.547 \log a - 18.96(\log a)^2 - 5.576(\log a)^3\right)/a \tag{60}$$

From S_3:

$$U_3 = \left(1.168 + 2.763 \log a - 0.629(\log a)^2 - 0.406(\log a)^3\right) \times 10^{-3}/a \tag{61}$$

$$V_3 = 2.731 \tag{62}$$

$$W_3 = -59.15 \tag{63}$$

Table 5. Results for $A = 15\,\mu m$ for the Fitted Parameters for the Continuous Variations of $\log(-S_1)$ as Functions of q in Terms of U_1, V_1, and W_1; of S_2 in Terms of U_2, V_2, W_2, and X_2; and of S_3 in Terms of U_3, V_3, and W_3 as in Equations (43)–(45)[a]

a (μm)	U_1	V_1	W_1	U_2	V_2	W_2	X_2	U_3	V_3	W_3
2.0	−0.289	1.025	−0.071	0.25	0.37	−0.73	0.23	0	-	-
1.5	−0.085	1.181	−0.182	0.22	0.17	−0.10	−0.11	0	-	-
1.0	0.228	1.264	−0.308	0.20	0.19	−0.27	−0.04	0	-	-
0.6	0.489	1.313	−0.406	0.10	0.06	−0.82	0.28	0	-	-
0.4	0.646	1.248	−0.394	0.04	0.15	−1.55	0.60	0	-	-
0.2	0.870	1.151	−0.347	−0.17	0.23	−2.44	0.80	-1.267×10^{-4}	2.523	−63.47
0.1	1.060	1.130	−0.323	−0.30	0.15	−4.71	1.14	-6.967×10^{-4}	2.523	−63.47
0.04	1.284	1.166	−0.322	−0.40	−0.35	−2.58	−5.84	-3.133×10^{-3}	2.523	−63.47
0.02	1.428	1.153	−0.272	−0.60	−5.09	17.33	−34.4	−0.01077	2.523	−63.47
0.01	1.564	1.145	−0.225	−0.95	−22.4	88.5	−113	−0.02667	2.523	−63.47
0.004	1.790	1.073	−0.157	−1.50	−65.6	258	−305	−0.06334	2.523	−63.47

[a]Indeterminate results are indicated by the hyphen symbol, and smoothing was as for $A = 6\,\mu m$.

2.5.2. Results for U, V, W, and X for $A = 15\,\mu m$

Table 5 gives the discrete results for U, V, W, and X for $A = 15\,\mu m$.

The overall fits of $H_{Q,q,A,a}$ in equation (46) to the corresponding $F_{Q,q,A,a} - F_{0,q,A,a}$ have standard deviations averaging 2.8% for $A = 15\,\mu m$ and a between 2 μm and 0.004 μm. For $a > 0.2\,\mu m$ the fits for S_1 and S_2 are made for Q values of $-200\,e$, $0\,e$, and $200\,e$, $0\,e$ for each q are exact; however, the fitted U, V, W, and X are not exact.

For $A = 15\,\mu m$ and for a between 2.0 μm and 0.4 μm the fitted expressions as continuous functions of a for U, V, W, and X are

From S_1:
$$U_1 = 0.213 - 1.488 \log a - 0.815(\log a)^2 + 0.514(\log a)^3 \tag{64}$$
$$V_1 = 1.279 - 0.389 \log a - 1.326(\log a)^2 - 0.428(\log a)^3 \tag{65}$$
$$W_1 = -0.310 + 0.629 \log a + 0.759(\log a)^2 - 0.737(\log a)^3 \tag{66}$$

From S_2:
$$U_2 = 0.187 + 0.314 \log a - 0.294(\log a)^2 - 0.347(\log a)^3 \tag{67}$$
$$V_2 = 0.125 + 0.395 \log a - 1.092(\log a)^2 + 0.060(\log a)^3 \tag{68}$$
$$W_2 = -0.181 + 1.799 \log a - 8.398(\log a)^2 - 10.928(\log a)^3 \tag{69}$$
$$X_2 = -0.071 - 1.040 \log a + 4.468(\log a)^2 + 7.270(\log a)^3 \tag{70}$$

From S_3: the values of U_3 are zero in this range, and the values for V_3 and W_3 are indeterminate.

For $A = 15\,\mu m$ and for a between 0.4 μm and 0.004 μm there is a rapid increase in S_2 and S_3 with decreasing a. The fitted expressions as functions of a for U, V, W, and X in the same format as for $A = 6\,\mu m$ in this range are

From S_1:
$$U_1 = 0.266 - 1.081 \log a - 0.353(\log a)^2 - 0.070(\log a)^3 \tag{71}$$
$$V_1 = 1.478 + 0.812 \log a + 0.612(\log a)^2 + 0.144(\log a)^3 \tag{72}$$
$$W_1 = -0.461 - 0.230 \log a - 0.141(\log a)^2 - 0.041(\log a)^3 \tag{73}$$

From S_2:
$$U_2 = 0.435 + 1.343 \log a + 0.922(\log a)^2 + 0.292(\log a)^3 \tag{74}$$
$$V_2 = \left(-0.320 - 0.326 \log a - 0.324(\log a)^2 - 0.061(\log a)^3\right)/a \tag{75}$$
$$W_2 = \left(-0.020 + 2.163 \log a + 2.194(\log a)^2 + 0.460(\log a)^3\right)/a \tag{76}$$
$$X_2 = \left(-0.404 - 2.355 \log a - 2.362(\log a)^2 - 0.514(\log a)^3\right)/a \tag{77}$$

Table 6. Results for $A = 3\ \mu m$ for the Fitted Parameters for the Continuous Variations of $\log(-S_1)$ in Terms of U_1, V_1, and W_1; of S_2 in Terms of U_2, V_2, W_2, and X_2; and of S_3 in Terms of U_3, V_3, and W_3 as in Equations (43)–(45)[a]

$a(\mu m)$	U_1	V_1	W_1	U_2	V_2	W_2	X_2	U_3	V_3	W_3
2.0	1.081	0.887	0.017	120	−30.6	123.1	−81.6	0	-	-
1.5	1.253	1.168	−0.174	117	−53.2	210.9	−158.3	-1.657×10^{-3}	2.917	−55.80
1.0	1.532	1.325	−0.327	92.3	−23.1	−6.2	−68.7	-1.088×10^{-2}	2.917	−55.80
0.6	1.813	1.325	−0.400	39.9	91.9	−449	127	-2.838×10^{-2}	2.917	−55.80
0.4	1.983	1.220	−0.371	14.6	92.2	−504	137	-6.627×10^{-2}	2.917	−55.80
0.1	2.344	1.088	−0.287	−42.6	−125	138	−950	-5.006×10^{-1}	2.917	−55.80
0.02	2.605	1.030	−0.186	−78.5	−1542	6076	−7120	−2.345	2.917	−55.80
0.008	2.655	0.990	−0.139	−154	−2676	9,665	−10,543	−2.808	2.917	−55.80

[a]Indeterminate results are indicated by the hyphen symbol, and smoothing was as for $A = 6\ \mu m$. The overall fits of $H_{Q,q,A,a}$ in equation (46) to the corresponding $F_{Q,q,A,a} - F_{0,q,A,a}$ have standard deviations averaging 3.6% for $A = 3\ \mu m$ and a between 2 μm and 0.008 μm.

From S_3:

$$U_3 = \left(-7.044 - 30.41 \log a - 39.30(\log a)^2 - 9.742(\log a)^3\right) \times 10^{-5}/a \tag{78}$$

$$V_3 = 2.523 \tag{79}$$

$$W_3 = -63.47 \tag{80}$$

2.5.3. Results for U, V, W, and X for $A = 3\ \mu m$

Table 6 gives the discrete results for U, V, and W for $A = 3\ \mu m$.

For $A = 3\ \mu m$ and for a between 2 μm and 0.4 μm the fitted expressions as continuous functions of a for U, V, and W in the same formats as for $A = 6\ \mu m$ in this range are

From S_1:

$$U_1 = 1.523 - 1.466 \log a - 0.369(\log a)^2 + 1.032(\log a)^3 \tag{81}$$

$$V_1 = 1.334 - 0.428 \log a - 2.781(\log a)^2 - 2.495(\log a)^3 \tag{82}$$

$$W_1 = -0.331 + 0.614 \log a + 1.507(\log a)^2 + 0.711(\log a)^3 \tag{83}$$

From S_2:

$$U_2 = 90.77 + 212.2 \log a - 197.3(\log a)^2 - 623.3(\log a)^3 \tag{84}$$

$$V_2 = -13.90 - 453.6 \log a - 574.9(\log a)^2 - 2600(\log a)^3 \tag{85}$$

$$W_2 = -12.15 + 1977 \log a - 2103(\log a)^2 - 9946(\log a)^3 \tag{86}$$

$$X_2 = -68.96 - 879.5 \log a + 1192(\log a) + 5281(\log a)^3 \tag{87}$$

From S_3:

$$U_3 = \left(-9.468 - 32.67 \log a - 9.532(\log a)^2 - 36.16(\log a)^3\right) \times 10^{-3}/a \tag{88}$$

$$V_3 = 2.917 \tag{89}$$

$$W_3 = -55.80 \tag{90}$$

For $A = 3\ \mu m$ and for a between 0.4 μm and 0.008 μm there is a rapid increase in S_2 and S_3 with decreasing a. The fitted expressions as continuous functions of a for U, V, and W in the same formats as for $A = 6\ \mu m$ in this range are

From S_1:

$$U_1 = 1.694 - 0.763 \log a - 0.083(\log a)^2 + 0.030(\log a)^3 \tag{91}$$

$$V_1 = 1.399 + 0.570 \log a + 0.332(\log a)^2 + 0.073(\log a)^3 \tag{92}$$

$$W_1 = -0.4153 - 0.0922 \log a + 0.0518(\log a)^2 + 0.0157(\log a)^3 \tag{93}$$

From S_2:

$$U_2 = 129.7 + 404.0 \log a + 326.3(\log a)^2 + 94.53(\log a)^3 \tag{94}$$

$$V_2 = -485.3 - 2297 \log a - 2249(\log a)^2 - 312.6(\log a)^3 \tag{95}$$

$$W_2 = 3426 + 15456 \log a + 15248(\log a)^2 + 3080(\log a)^3 \tag{96}$$

$$X_2 = -3522 - 14884 \log a - 15610(\log a)^2 - 3298(\log a)^3 \tag{97}$$

From S_3:

$$U_3 = \left(-489.6 + 5605 \log a + 8.813(\log a)^2 - 1080(\log a)^3 \right) \times 10^{-5}/a \tag{98}$$

$$V_3 = 2.917 \tag{99}$$

$$W_3 = -55.8 \tag{100}$$

3. Worked Examples of Use of Parameterization

Worked examples for droplet radius $A = 6\,\mu m$, particle radius $a = 0.8\,\mu m$, particle charge $q = 10\,e$, droplet charges $Q = 50\,e$ and $Q = -50\,e$, pressure 540 hPa, temperature $= -17°C$ (256.15 K), and relative humidity 100%.

To get $P_{0,0,A,a} = P_{C,A,a} + R_{F,A,a}$ as in equation (15),

insert $A = 6\,\mu m$ in equations (12)–(14), giving $P_{C,6,8} = 1.6455 \times 10^{-14}\,m^3\,s^{-1}$,
droplet fall speed $U_\infty = 4.910 \times 10^{-3}\,m\,s^{-1}$,
Knudsen number $N_{Kn} = 1.302 \times 10^{-1}$, and
particle mobility $B_p = 4.7328 \times 10^9\,s\,kg^{-1}$ so that
particle diffusion coefficient $D_p = 1.6735 \times 10^{-11}\,m^2\,s^{-1}$ giving $f_p = 8.4982$,
so $R_{F,6,8} = 4\pi \times 1.6735 \times 10^{-11} \times 8.4982 \times 6 \times 10^{-6} \times 10^{-14}\,m^3\,s^{-1} = 1.0723 \times 10^{-14}\,m^3\,s^{-1}$, and
so $P_{0,0,6,8} = (1.0723 + 1.6455) \times 10^{-14}\,m^3\,s^{-1} = 2.718 \times 10^{-14}\,m^3\,s^{-1}$.

From equations (18)–(21) and (17):

$$K = -2.8733; \quad L = 1.5844; \quad M = -0.6053; \quad \text{and} \quad N = -0.3579, \quad \text{giving}$$

$$G_{0,10,6,.8} = 10^{**}(-1.0415) = 0.090887$$

From equations (47) to (53) and (46):

$$U_1 = 1.1686; \quad V_1 = 1.1483; \quad \text{and} \quad W_1 = -0.2814, \quad \text{giving} \quad \log(-S_1) = 2.0355$$

$$U_2 = 4.6604; \quad V_2 = 6.1714; \quad W_2 = -21.5518; \quad \text{and} \quad X_2 = 4.3094, \quad \text{giving} \quad S_2 = -6.4106$$

For droplet charge $Q = 50\,e$,

$$H_{50,,10,6,.8} = -10^{-5} \times 50 \times 10^{**}(2.0355) + 10^{-7} \times 50^2 \times (-6.4106) = -0.055861$$

and from equation (2)

$$P_{50,10,6,.8} = P_{0,0,6,.8} \times 10^{**}(-0.055861 + 0.090887)$$

$$P_{50,10,6,.8} = P_{0,0,6,.8} \times 1.0840$$

$$P_{50,10,6,.8} = 2.946 \times 10^{-14}\,m^3\,s^{-1}$$

For droplet charge $Q = -50\,e$:

$$H_{-50,10,6,.8} = 10^{-5} \times 50 \times 10^{**}(2.0355) + 10^{-7} \times 50^2 \times (-6.4106) = -0.052656$$

$$P_{-50,10,6,.8} = P_{0,0,6,.8} \times 10^{**}(0.055861 + 0.090887)$$

$$P_{-50,10,6,.8} = P_{0,0,6,.8} \times 1.4020$$

$$P_{-50,10,6,.8} = 3.811 \times 10^{-14}\,m^3\,s^{-1}$$

Also, for droplet charge $Q = 0\,e$:

$$H_{0,10,6,.8} = 0$$

$$P_{0,10,6,.8} = P_{0,0,6,.8} \times 10^{**}(0.090887)$$

$$P_{0,10,6,.8} = P_{0,0,6,.8} \times 1.2328\,m^3\,s^{-1}$$

$$P_{0,10,6,.8} = 3.351 \times 10^{-14}\,m^3\,s^{-1}$$

We see that the effect of the charge q of $10\,e$ on the aerosol particle alone is to increase the scavenging rate by a factor of 1.23 over the uncharged rate. For the droplet charge Q of $50\,e$, even with long-range repulsion, there is still an increase by a factor of 1.08, while for Q of $-50\,e$, with long-range attraction, the increase is by a factor of 1.40. For droplets of radii other than $15\,\mu m$, $6\,\mu m$, or $3\,\mu m$, a spline interpolation or moderate extrapolation of results for these three droplet radii can be made.

4. Discussion

These parameterizations provide inputs for use in modeling scavenging rates in realistic models of cloud formation and development. A prior model of the amount of electric charge on the nuclei and droplets throughout the cloud is needed, but observations provide a starting point, and prior modeling and outlines of the processes of can provide some guidance [*Zhou and Tinsley*, 2007, 2012; *Vonnegut et al.*, 1962; *Tinsley*, 2012].

The amount of energy density in the global electric circuit, and the amount of energy density that is involved in changing the scavenging rates, is many orders of magnitude less than that involved in the macroscopic changes in atmospheric dynamics observed in response to global atmospheric electrical changes [*Tinsley*, 2000; *Lam et al.*, 2013; *Harrison and Ambaum*, 2013]. Thus, there is a question as to how variations in these very small energy inputs can be amplified to account for the correlated macroscopic meteorological changes (which are still small in meteorological terms). Two such situations where diversion of meteorological energy flow can be modulated by electric charge, as the charge affects the scavenging of particles by droplets, are as follows:

Amplification in storm invigoration—the electroscavenging of large aerosol particles and the electroantiscavenging of small aerosol particles in clouds, changes the concentration and size distribution of the subset of the particles active as cloud condensation nuclei (CCN). As noted, the lifetimes of such particles, and therefore of variations in size distribution, are 1–10 days. In subsequent episodes of updrafts, cooling and condensation occur, and the result is changes in the droplet size distribution due to changes in the CCN size distribution. With larger numbers of smaller CCN and fewer numbers of large CCN the available water vapor is converted into larger numbers of smaller droplets and smaller numbers of larger droplets. Both of these changes inhibit coagulation, and reduce the amount of initial precipitation, so that more liquid water is carried above the freezing level. As it freezes it releases more latent heat of freezing, which invigorates the updraft. Electrically induced increases in collision rates (electroscavenging) of ice forming nuclei (IFN) with liquid droplets above the freezing level can also increase the latent heat release.

Amplification by variations in cloud albedo, cloud cover, and infrared opacity is applicable to layer clouds where the concentration and size distribution of droplets, again due to electrically induced changes in CCN and IFN processes, directly affect albedo and infrared opacity and indirectly affect cloud cover because of changes in drizzle production and cellular structure in broken clouds. The balance between long-wave and short-wave radiation is changed, affecting surface temperature, and again a large amplification of the small electrical energy input occurs.

In both of these situations, the action of the CCN and IFN can be viewed as that of catalysts for the partitioning or diversion of the energy flows. It is thus possible for the very small electrical inputs to be amplified into much larger changes in meteorological energy flow as they modulate the catalytic action of the nuclei. There are a number of separate pathways by which this can occur:

Pathway 1: IFN in contact ice nucleation. IFN are generally larger than $0.5\,\mu m$ radius; electroscavenging increases the collision rate independent of the sign of Q/q. As droplets cool in updrafts contact ice nucleation occurs at around $-5°C$, in advance of other droplet freezing processes when the updrafts cool to around $-15°C$. Thus, especially for clouds with slow updrafts, increases can occur in initial ice production, latent heat of freezing, and increased updraft speed (storm invigoration). For layer clouds there may be cloud cover changes.

Pathway 2: CCN concentrations and size distributions. Increases in electroscavenging for CCN larger than about $0.3\,\mu m$ radius decrease their concentration independent of the sign of Q/q. With space charge present, decreases in electroantiscavenging for smaller CCN result in concentrations remaining higher than without space charge. As noted earlier, changes in droplet size distribution can be produced in later cycles of evaporation/condensation which reduce coagulation and initial precipitation and increase latent heat release above the freezing level. The resulting invigoration can increase the vorticity of baroclinic storms. It may also

increase the amount of water released into the upper troposphere, increase the production of lightning, and change cloud cover.

Pathway 3: evaporation nuclei as CCN. Droplets, with their large size, carry much more charge than nuclei, and when droplets evaporate, the "evaporation nuclei" retain that charge for 10 min or so. Evaporation of charged droplets occurs in downdrafts and in air entrained by turbulence near cloud boundaries and results in highly charged evaporation nuclei [*Beard*, 1992] with the higher electric charge producing a greater modulation of scavenging, with macroscopic consequences enhanced in comparison to those for smaller charges.

Pathway 4: evaporation nuclei as IFN. Turbulence and entrainment at cloud tops, if above the freezing level, can result in highly charged evaporation nuclei that can act as IFN in the contact ice nucleation mode. The material absorbed by the droplet during its lifetime stays with it as it shrinks by evaporation, and on the surface of the former CCN can activate it as an IFN, promoting freezing [*Rosinsky and Morgan*, 1991]. The electrical enhancement of this effect would have similar macroscopic consequences to those described earlier.

Pathway 5: in-cloud scavenging of immersion IFN. The particles that act as IFN but are not effective as CCN are left as interstitial particles when cloud droplets are condensing on CCN. The interstitial IFN can be electroscavenged into droplets below the freezing level, and later act as immersion freezing nuclei above the −15°C level, with similar macroscopic consequences to those described earlier.

More speculative pathways involve modulating the process of ion-mediated nucleation forming ultrafine particles [*Kirkby et al.*, 2011]. For example, on particles nucleated near cloud boundaries with volatiles released from evaporating droplets, electroantiscavenging may protect the ultrafine nuclei from coagulation with ambient particles as they grow by vapor deposition into CCN, thus increasing the ultimate concentration of CCN.

5. Conclusions and Implications

Simulations of the effects of electric charge in increasing loss rates for large cloud condensation nuclei and ice forming nuclei, and decreasing loss rates for small nuclei, have been made for a wide range of aerosol particle radii, and particle and droplet charges, as typical for clouds immersed in the global ionization produced by galactic cosmic rays. Consequences of the microphysical changes for macroscopic changes in precipitation, atmospheric dynamics related to latent heat partitioning, and cloud cover have been explored.

Such consequences provide an explanation for many observations of atmospheric dynamical changes related to changes in atmospheric ionization, both those induced externally [*Tinsley*, 2000; *Lam et al.*, 2013] and those induced internally [*Burns et al.*, 2008; *Harrison and Ambaum*, 2013]. It should be noted that the small atmospheric responses are observed for changes in J_z, of only tens of percent, implying that the mean level of J_z causes continual effects in basic aerosol-cloud physics that are 5 or more times larger. With increases in J_z expected with global warming, and a possible doubling at high latitudes during another Maunder Minimum of solar activity and maximum of cosmic ray flux, effects on clouds and climate could be much greater, especially for the electroscavenging of the larger nuclei, which varies approximately with the square of the particle charge.

Uncertainties remain as to which of a number of microphysical pathways connect the electrically modulated changes in scavenging rates to macroscopic cloud and dynamical changes. The present simulations have been parameterized for rapid use in cloud models with detailed microphysics. Together with models of the charging processes in clouds, the parameterized changes in scavenging caused by the electric charges can be used to test the relative importance of the various pathways and quantitatively test the overall macroscopic effects on clouds. If they provide quantitative agreement with observations of weather and climate responses to atmospheric ionization changes, they could eventually be used in global models for forecasting such contributions to weather and climate changes.

Appendix A

The discrete results of the simulations are given in numerical form in Tables A1, A2, and A3 for droplet radii 15 μm, 6 μm, and 3 μm, respectively.

Table A1. Simulations of $R_{Q,q,A,a}$ for Droplet Radius $A = 15\mu m$, Particle Radius a[a]

a	−200,2	−100,2	−50,2	0,2	50,2	100,2	200,2
2	42.52			42.22			42.12
1.5	28.16			27.87			27.22
1	18.72			18.4			18.11
0.6	15.60			15.13			14.71
0.4	17.08			16.32			15.64
0.2	26.69		25.53	24.95	24.78		23.16
0.1	53.03		49.45	48.11	46.70		42.77
0.04	169.1	156.5	149.6	142.5	137.3	131.8	120.0
0.02	461.1	407.3	384.1	358.6	337.5	315.2	274.9
0.01	1356	1141	1050	954.8	866.8	796.2	643.3
0.004	6395	4976	4322	3837	3389	2898	2102
a	−200,5	−100,5	−50,5	0,5	50,5	100,5	200,5
2	43.04			42.42			41.98
1.5	28.69			28.09			27.61
1	19.76			18.89			18.19
0.6	17.72			16.40			15.41
0.4	20.64			18.68			16.90
0.2	35.01		31.60	30.36	29.27		26.29
0.1	73.28		62.58	57.77	55.41		46.78
0.04	240.4	203.4	185.3	168.2	153.0	141.0	110.9
0.02	694.6	537.0	466.6	410.5	350.3	309.3	211.7
0.01	2191	1590	1287	1054	862.2	659.3	388.1
0.004	11430	7150	5428	4060	2837	1926	799.7
a	−200,10	−100,10	−50,10	0,10	50,10	100,10	200,10
2	43.63			42.81			42.06
1.5	30.09			28.89			27.88
1	22.29			20.74			19.27
0.6	23.52			20.68			18.29
0.4	29.87			25.37			22.12
0.2	53.83		46.20	43.54	41.66		34.43
0.1	113.8		88.82	81.87	74.67		57.42
0.04	377.6	292.7	253.1	219.3	189.9	156.9	107.4
0.02	1129	816.5	641.3	509.1	406.3	299.4	151.7
0.01	3756	2408	1722	1225	886.9	519.5	172.5
0.004	20980	11460	7669	4581	2356	1060	149.4
a	200,20	100,20	50,20	0,20	50,20	100,20	200,20
2	46.18			44.41			42.64
1.5	34.29			31.92			29.88
1	30.9			27.59			24.59
0.6	39.67			34.33			29.25
0.4	53.19			44.71			36.85
0.2	96.0		79.54	74.37	69.70		55.3
0.1	198.6		144.9	134.5	122.8		83.32
0.04	684.7	502.3	416.1	337.7	266.9	215.8	116
0.02	2056	1359	1017	714.9	507.1	317.4	92.15
0.01	7047	4065	2751	1648	952.2	369.7	38.52
0.004	40470	20750	12440	5687	1767	362.2	2
a	−200,50	−100,50	−50,50	0,50	50,50	100,50	200,50
2	59.77			55.13			50.87
1.5	57.07			51.43			46.03
1	68.07			60.24			52.88
0.6	95.58			82.24			69.73
0.4	129.9			107.2			87.05
0.2	231.5		188.6	175.1	164.5		125.6
0.1	475.8		347.9	308.4	275.7		174.6
0.04	1563	1170	894.9	697.7	559.7	400.9	157.2
0.02	4770	3068	2110	1398	853.3	409.6	38.78

Table A1. (continued)

a	−200,50	−100,50	−50,50	0,50	50,50	100,50	200,50
0.01	16770	9345	5761	2927	1068	207.3	1
0.004	97380	48430	27360	8941	947.4	23	0.01

a	Ventilated Brownian	0,0
2	3.27	42.14
1.5	4.02	27.83
1	5.43	18.30
0.6	8.05	14.89
0.4	11.22	15.81
0.2	20.99	23.68
0.1	43.73	45.06
0.04	134	134.4
0.02	340	341
0.01		918.9
0.004		3773

[a] −200,2 means $Q = -200$, $q = 2$. Units are $10^{-14} \, \mathrm{m^3 \, s^{-1}}$.

Table A2. Simulations of $R_{Q,q,A,a}$ for Droplet Radius $A = 6 \, \mu m$, Particle Radius a[a]

a	−100,2	−50,2	−25,2	0,2	25,2	50,2	100,2
	6.944			6.667			6.743
1.5	4.700			4.484			4.477
1	3.220			3.031			2.926
0.6	2.790			2.533			2.325
0.4	3.146	2.947	2.854	2.775	2.688	2.618	2.438
0.2	5.257	4.786	4.533	4.349	4.107	3.917	3.538
0.1	11.34	9.928	9.257	8.615	8.015	7.437	6.322
0.04	41.43	34.20	30.19	27.14	24.20	21.86	16.55
0.02	130.7	102.1	86.13	73.78	63.25	54.06	36.62
0.01	443.5	323.9	268.5	221.0	178.3	143.0	88.97
0.004	2508	1711	1395	1100	855.5	643.3	357.6

a	−100,5	−50,5	−25,5	0,5	25,5	50,5	100,5
2	7.085			6.698			6.632
1.5	4.903			4.517			4.348
1	3.539			3.115			2.801
0.6	3.395			2.750			2.21
0.4	4.184	3.641	3.421	3.171	2.953	2.742	2.346
0.2	7.736	6.546	5.931	5.309	4.722	4.236	3.333
0.1	18.50	14.60	12.31	10.54	9.014	7.724	5.244
0.04	74.20	51.96	40.67	31.88	24.63	19.08	9.489
0.02	249.2	162.9	116.8	84.17	58.08	37.67	14.61
0.01	891.6	531.2	376.2	245.8	148.1	84.95	21.67
0.004	5280	2961	1999	1194	654.4	289.5	58.08

a	−100,10	−50,10	−25,10	0,10	25,10	50,10	100,10
2	7.388			6.783			6.489
1.5	5.321			4.652			4.221
1	4.268			3.435			2.750
0.6	4.867			3.501			2.380
0.4	6.597	5.540	4.949	4.433	3.949	3.511	2.698
0.2	13.23	10.47	8.976	7.659	6.483	5.433	3.614
0.1	31.70	22.82	18.32	14.68	11.43	8.885	4.494
0.04	140.9	83.40	60.55	41.66	26.66	15.74	4.204
0.02	470.3	268.5	175.1	103.9	55.72	23.76	2.855
0.01	1669	942.3	574.2	292.7	112.6	35.76	1.915
0.004	10120	5327	3089	1357	429.8	84.01	3

Table A2. (continued)

a	−100,20	−50,20	−25,20	0,20	25,20	50,20	100,20
2	8.166			7.058			6.34
1.5	6.489			5.212			4.216
1	6.330			4.622			3.187
0.6	8.600			5.839			3.495
0.4	12.25	9.843	8.749	7.687	6.744	5.714	4.076
0.2	24.87	18.53	15.64	12.94	10.53	8.348	4.801
0.1	60.19	41.03	31.89	23.80	17.09	11.61	4.118
0.04	260.4	154.0	102.9	62.40	32.18	13.19	1.070
0.02	886.0	476.9	288.3	145.3	49.16	10.07	0.147
0.01	3187	1620	968.3	373.4	72.45	7.961	0.02
0.004	18480	9406	5054	1665	206	11.48	

a	−100,50	−50,50	−25,50	0,50	25,50	50,50	100,50
2	11.5			9.019			6.977
1.5	11.5			8.562			5.995
1	14.21			10.12			6.626
0.6	21.00			13.96			8.096
0.4	30.16	24.16	21.12	18.24	15.71	13.33	9.096
0.2	60.21	44.17	36.82	29.89	23.61	18.06	9.111
0.1	149.2	97.25	72.95	52.61	35.09	21.54	4.563
0.04	641.6	352	226	122.4	48.65	11.20	0.029
0.02	2081	1091	643.2	250.2	43.07	1.62	0.001
0.01	7791	4008	2155	593.5	30.9	0.3	0.0001
0.004	42820	22900	12010	2438	33.8	0.01	

a	Ventilated Brownian	0,0					
2	0.5406	6.673					
1.5	0.6668	4.475					
1	0.9033	3.012					
0.6	1.348	2.489					
0.4	1.892	2.697					
0.2	3.594	4.136					
0.1	7.690	8.095					
0.04	25.02	25.56					
0.02	68.94	69.92					
0.01		213.0					
0.004		1062					

[a]−100,2 means $Q = -100\,e$, $q = 2\,e$. Units are $10^{-14}\,m^3\,s^{-1}$.

Table A3. Simulations of $R_{Q,q,A,a}$ for Droplet Radius $A = 3\,\mu m$, Particle Radius a[a]

a	−50,2	−25,2	−10,2	0,2	10,2	25,2	50,2
2	1.862			1.708			1.789
1.5	1.333		1.215	1.195	1.186		1.273
1	0.940		0.838	0.823	0.811		0.796
0.6	0.826		0.726	0.695	0.678		0.605
0.4	0.959	0.861	0.803	0.769	0.736	0.687	0.616
0.1	3.931	3.222	2.760	2.533	2.270	1.949	1.474
0.02	55.06	39.99	31.45	26.60	21.93	16.68	9.849
0.008	303.7	207.1	160.8	133.7	108.8	73.26	41.40

a	−50,10	−25,10	−10,10	0,10	10,10	25,10	50,10
2.0	2.071			1.728			1.656
1.5	1.600		1.295	1.235	1.194		1.077
1	1.362		0.990	0.916	0.853		0.621
0.6	1.643		1.065	0.928	0.816		0.446

Table A3. (continued)

a	−50,10	−25,10	−10,10	0,10	10,10	25,10	50,10
0.4	2.335	1.720	1.393	1.185	1.005	0.762	0.472
0.1	13.21	8.544	5.666	4.195	3.077	1.636	0.447
0.02	225.9	119.6	64.79	37.70	18.24	4.653	0.251
0.008	1260	666.5	346.1	180.8	76.70	15.22	0.30

a	−50,20	−25,20	−10,20	0,20	10,20	25,20	50,20
2	2.392			1.791			1.547
1.5	2.029		1.662	1.354	1.263		0.974
1	2.097		1.374	1.209	1.058		0.593
0.6	2.978		1.772	1.516	1.274		0.514
0.4	4.402	3.124	2.440	2.011	1.631	1.170	0.554
0.1	25.53	15.15	9.718	6.514	4.039	1.568	0.134
0.02	419.2	215.8	111.7	50.12	15.50	1.265	0.001
0.008	2450	1275	586.1	230.4	54.10	2.351	-

a	−50,50	−25,50	−10,50	0,50	10,50	25,50	50,50
2	3.538			2.242			1.463
1.5	3.625		2.415	2.142	1.888		1.055
1	4.616		2.910	2.534	2.166		0.992
0.6	7.153		4.150	3.507	2.898		1.009
0.4	10.67	7.495	5.656	4.601	3.763	2.455	0.933
0.1	63.06	36.54	21.52	13.39	7.092	1.865	0.011
0.02	941.5	528.8	238.0	79.13	9.960	0.414	-
0.008	5429	2891	1279	342.9	20.78	0.013	-

a	Ventilated Brownian	0,0
2	0.141	1.707
1.5	0.175	1.193
1	0.245	0.815
0.6	0.361	0.684
0.4	0.512	0.749
0.1	2.230	2.362
0.02	24.49	24.99
0.008		124.3

[a]−50,2 means $Q = -50\,e$, $q = 2\,e$. Units are $10^{-14}\,\mathrm{m}^3\,\mathrm{s}^{-1}$.

References

Beard, K. V. (1992), Ice initiation in warm-based convective clouds: An assessment of microphysical mechanisms, *Atmos. Res., 28*, 125–152.

Beard, K. V., and H. R. Pruppacher (1969), A determination of the terminal velocity and drag of small water drops by means of a wind tunnel, *J. Atmos. Sci., 26*, 1006–1072.

Burns, G. B., B. A. Tinsley, W. J. R. French, O. A. Troshichev, and A. V. Frank-Kamenetsky (2008), Atmospheric circuit influences on ground-level pressure in the Antarctic and Arctic, *J. Geophys. Res., 113*, D15112, doi:10.1029/2007JD009618.

Davis, M. H. (1964a), Two charged spherical conductors in a uniform electric field: Forces and field strength, RM-3860-PR, The RAND Corp., Santa Monica, Calif.

Davis, M. H. (1964b), Two charged spherical conductors in a uniform electric field: Forces and field strength, *Q. J. Mech. Appl. Math. 17*, 400–511.

Harrison, R. G., and M. H. P. Ambaum (2013), Electrical signature in polar night cloud base variations, *Environ. Res. Lett., 8*, 015027.

Hoppel, W. A., and G. F. Frick (1986), Ion-aerosol attachment coefficients and the steady-state charge distributions on aerosols in a bipolar ion environment, *Aerosol Sci. Technol., 5*, 1–21.

Keefe, D., P. J. Nolan, and J. A. Scott (1968), Influence of Coulomb and image forces on combination in aerosols, *Proc. R. Ir. Acad., Sect. A, 66*, 17–24.

Khain, A., V. Arkhipov, M. Pinsky, Y. Feldman, and Y. Ryabov (2004), Rain enhancement and fog elimination by seeding with charged droplets. Part I: Theory and numerical simulations, *J. Appl. Meteorol., 43*, 1513–1529.

Kirkby, J., et al. (2011), Role of sulfuric acid, ammonia and galactic cosmic rays in atmospheric nucleation, *Nature, 476*, 429–433, doi:10.1038/nature10343.

Lam, M. M., G. Chisham, and M. P. Freeman (2013), The interplanetary field influences mid-latitude surface atmospheric pressure, *Environ. Res. Lett., 8*, 045001.

Pruppacher, H. R., and R. Jaenike (1995), The processing of water vapor and aerosols by atmospheric clouds, a global estimate, *Atmos. Res., 38*, 283–295.

Pruppacher, H. R., and J. D. Klett (1997), *Microphysics of Clouds and Precipitation*, 2nd ed., 954 pp., Springer, New York.

Rosenfeld, D., Y. K. Kaufman, and I. Koren (2006), Switching cloud cover and dynamical regimes from open to closed Bernal cells in response to suppression of precipitation by aerosols, *Atmos. Chem. Phys., 6*, 2503–2511.

Rosenfeld, D., U. Lohman, G. B. Raga, C. D. O'Dowd, M. Kumala, S. Fuzzi, A. Reissell, and M. O. Andrease (2008), Flood or drought: How do aerosols affect precipitation?, *Science, 321*, 1309–1313.

Rosinsky, J., and G. Morgan (1991), Cloud condensation nuclei as a source of ice-forming nuclei in clouds, *J. Aerosol Sci.*, *22*, 123–133.

Tao, W. K., J. P. Chen, Z. Li, C. Wang, and C. Zhang (2012), Impact of aerosols on convective clouds and precipitation, *Rev. Geophys.*, *50*, RG2001, doi:10.1029/2011RG000369.

Tinsley, B. A. (2000), Influence of the solar wind on the global electric circuit and inferred effects on cloud microphysics, temperature and dynamics of the troposphere, *Space Sci. Rev.*, *94*, 231–258.

Tinsley, B. A. (2010), Electric charge modulation of aerosol scavenging in clouds: Rate coefficients with Monte-Carlo simulations of diffusion, *J. Geophys. Res.*, *115*, D23211, doi:10.1029/2010JD014580.

Tinsley, B. A. (2012), A working hypothesis for connections between electrically induced changes in cloud microphysics and storm vorticity, with possible effects on circulation, *Adv. Space Res.*, *50*, 791–805.

Tinsley, B. A., and D. B. Leddon (2013), Charge modulation of scavenging in clouds: Extension of Monte-Carlo simulations and initial parameterization, *J. Geophys. Res. Atmos.*, *118*, 8612–8624, doi:10.1002/jgrd.50618.

Tinsley, B. A., and L. Zhou (2014), Comments on "Effect of electric charge on collisions between cloud droplets", *J. Appl. Meteorol. Climatol.*, *53*(5), 1317–1320.

Tinsley, B. A., L. Zhou, and A. Plemmons (2006), Changes in scavenging of particles by droplets due to weak electrification in clouds, *Atmos. Res.*, *79*, 266–295.

Tripathi, S. N., S. Vishnoi, S. Kumar, and R. G. Harrison (2006), Computationally efficient expressions for the collision efficiency between electrically charges aerosol particles and cloud droplets, *Q. J. R. Meteorol. Soc.*, *132*, 1717–1731.

Vonnegut, B., C. B. Moore, R. G. Semonin, J. W. Bullock, D. W. Stags, and W. E. Bradley (1962), Effects of atmospheric space charge on initial electrification of cumulus clouds, *J. Geophys. Res.*, *67*, 3909–3922, doi:10.1029/JZ067i010p03909.

Wang, P. K., S. N. Grover, and H. R. Pruppacher (1978), On the effects of electric charge on scavenging of aerosol particles by clouds and small raindrops, *J. Atmos. Sci.*, *35*, 1735–1743.

Young, K. C. (1993), *Microphysical Processes in Clouds*, Oxford Univ. Press, U. K.

Zhou, L., and B. A. Tinsley (2007), Production of space charge at the boundaries of layer clouds, *J. Geophys. Res.*, *112*, D11203, doi:10.1029/2006JD007998.

Zhou, L., and B. A. Tinsley (2012), Time dependent charging of layer clouds in the global electric circuit, *Adv. Space Res.*, *50*, 828–842.